Suppression of auto-fluorescence from high-resolution 3D polymeric architectures fabricated via two-photon polymerization for cell biology applications

Sharaf, A.; Accardo, A.; Frimat, J.P.; Kremers, G.J.

MNE 19 (2023) 100188

Contents lists available at ScienceDirect

Micro and Nano Engineering

journal homepage: www.sciencedirect.com/journal/micro-and-nano-engineering

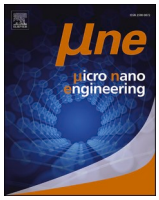

Suppression of auto-fluorescence from high-resolution 3D polymeric architectures fabricated via two-photon polymerization for cell biology applications

A. Sharaf [a,*], J.P. Frimat [b], G.J. Kremers [c], A. Accardo [a,*]

[a] Department of Precision and Microsystems Engineering, Faculty of Mechanical, Maritime and Materials Engineering (3mE), Delft University of Technology, Mekelweg 2, 2628 CD Delft, the Netherlands
[b] Department of Human Genetics, Leiden University Medical Center, 2333 ZA Leiden, the Netherlands
[c] Erasmus Optical Imaging Centre, Erasmus MC, 3015 GE Rotterdam, the Netherlands

ARTICLE INFO

Keywords:
Two-photon polymerization
Cell engineered microenvironments
Auto-fluorescence suppression
UV-bleaching
Auto-fluorescence quenching
Fluorescence microscopy

ABSTRACT

Two-photon polymerization (2PP) has provided the field of cell biology with the opportunity to fabricate precisely designed microscaffolds for a wide range of studies, from mechanobiology to *in vitro* disease modelling. However, a multitude of commercial and in-house developed photosensitive materials employed in 2PP suffers from high auto-fluorescence in multiple regions of the spectrum. In the context of *in vitro* cell biological studies, this is a major problem since one of the main methods of characterization is fluorescence microscopy of immunostained cells. This undesired auto-fluorescence of microscaffolds affects the efficiency of such an analysis as it often overlaps with fluorescent signals of stained cells rendering them indistinguishable from the scaffolds. Here, we propose two effective solutions to suppress this auto-fluorescence and compare them to determine the superiority of one over the other: photo-bleaching with a powerful UV point source and auto-fluorescence quenching via Sudan Black B (SBB). The materials used in this study were all commercially available, namely IP-L, IP-Dip, IP-S, and IP-PDMS. Bleaching was shown to be 61.7–92.5% effective in reducing auto-fluorescence depending on the material. On the other hand, SBB was shown to be 33–95.4% effective. The worst result in presence of SBB (33%) was in combination with IP-PDMS since the adsorption of the material on IP-PDMS was not sufficient to fully quench the auto-fluorescence. However, auto-fluorescence reduction was significantly enhanced when activating the IP-PDMS structures with oxygen plasma for 30 s. Moreover, we performed a cell culture assay using a human neuroblastoma cell line (SH-SY5Y) to prove the effectiveness of both methods in immunofluorescence characterization. SBB presented a lower performance in the study especially in presence of 2PP-fabricated microchannels and microcages, within which the differentiated SH-SY5Y cells migrated and extended their axon-like processes, since the SBB obstructed the fluorescence of the stained cells. Therefore, we concluded that photo-bleaching is the optimal way of auto-fluorescence suppression. In summary, this study provides a systematic comparison to answer one of the most pressing issues in the field of 2PP applied to cell biology and paves the way to a more efficient immunofluorescence characterization of cells cultured within engineered *in vitro* microenvironments.

1. Introduction

Additive manufacturing techniques have grown rapidly in the last few decades. With multiple achievable scales and geometries [1], they have become a true asset in fields like optics [2], microfluidics [3], and cell biology [4,5]. Technologies like electrospinning [6], stereolithography [7], bioprinting [8], and two-photon polymerization (2PP) [9] have opened the door to a new era of fundamental cell biology studies using micro and nanostructures that were not achievable before. Among these, 2PP especially stands out due to its many advantages. In 2PP, a photosensitive resin (or photoresin) is exposed to near infrared (NIR) laser to fabricate 3D complex free standing polymeric structures designed by a computer aided design (CAD) software with a resolution that can reach up to 50 nm [10,11]. This technology has been used

* Corresponding authors.
E-mail addresses: a.m.s.e.sharaf@tudelft.nl (A. Sharaf), a.accardo@tudelft.nl (A. Accardo).

https://doi.org/10.1016/j.mne.2023.100188
Received 19 December 2022; Received in revised form 24 February 2023; Accepted 8 April 2023
Available online 11 April 2023

increasingly in recent years to fabricate microscaffolds for biological studies due to its high reproducibility, controllability and achievable feature resolution [12–20]. The freedom of design provided by 2PP plays a major role in creating structures that can be employed to perform *in vitro* studies within the field of mechanobiology of various cell types. Mechanobiology is the study of the interactions of cells with the surrounding environment from a mechanical perspective. Structures such as nano-pillars [16,21], micro-cages [13,17,22], micro-towers [23], and submicrometric ridges [24] have been fabricated to study their effect on primary microglia, murine macrophages, human glioblastoma, patient-derived glioma cells, human neuroblastoma, human pluripotent stem cell-derived neurons, and rat neuroblastoma, respectively.

To perform such *in vitro* studies, one of the main techniques of characterization is fluorescence microscopy such as epifluorescence, confocal, two-photon, light-sheet or super-resolution microscopy. In order for this technique to be most efficient, there has to be minimal fluorescent background noise from any structures the cells are cultured on. In other words, the structures need to be non-auto-fluorescent. Unfortunately, auto-fluorescence is a major problem with multiple photoresins used in 2PP. This hinders the full capacity of analysis that can be carried out when using fluorescence microscopy since there is an area of the emission spectrum that is blocked by the auto-fluorescence of the fabricated scaffolds. Strong emission of the structures makes the visualization and therefore the analysis of stained cells challenging. This becomes especially a problem when working with 3D complex architectures since their large volumes lead to strong emission, thereby blocking any cells from view [16,25]. To mitigate this problem, multiple solutions have been devised by different research groups. These solutions can be divided into pre-processing or post-processing ones. An effective pre-processing solution consists of eliminating the auto-fluorescence of a photoresin before fabricating the structure (i.e. before exposing it to the NIR laser). Since, usually, the auto-fluorescent component of a photoresin is the photoinitiator, this is achieved by substituting the photoinitiator with a non-auto-fluorescent one [20] or one with very weak auto-fluorescence [23]. This method can be very effective in eliminating the majority of auto-fluorescence, however it has the disadvantage of being an ad-hoc solution which requires a lot of trial and error for each monomer solution. Post-processing solutions, on the other hand, come into effect after the fabrication of the structure. The two major methods within this category are photo-bleaching and auto-fluorescence quenching. Photo-bleaching takes place by exposing the structures to ultraviolet (UV) light for an extended amount of time [14] while quenching is achieved through coating the structures with a fluorescence-quenching material that absorbs emitted photons from the structures, such as Sudan Black B (SBB), one of the most commonly used fluorescence quenchers [20,25,26]. Even though there have been examples in literature of successfully using such post-processing solutions to eliminate the auto-fluorescence of 2PP-fabricated structures, there have been no systematic studies on the effect of each of these solutions compared to the other.

In the current study, we present a comparison of bleaching and quenching of the auto-fluorescence of multiple commercial photoresins (IP-L, IP-Dip, IP-S, and IP-PDMS) widely used in 2PP. In order to achieve this purpose in the most efficient manner, a square pedestal design was chosen due to the low fabrication time and because it enabled the most uniform way of testing the auto-fluorescence and the mechanical strength of the selected materials. The structures were characterized by scanning electron microscopy (SEM) and confocal microscopy. In addition, characterization of the mechanical strength of the structures after bleaching is also reported. Finally, as a proof of principle, human neuroblastoma cells (SH-SY5Y cell line) were cultured, differentiated, and stained on multiple 3D microscaffolds, fabricated by 2PP and treated with the aforementioned methods, to compare their efficiency as solutions to the problem of auto-fluorescence.

2. Materials and methods

2.1. Materials

Four proprietary acrylate based photoresins of Nanoscribe GmbH & Co. KG were used, namely IP-L, IP-Dip, IP-S, and IP-PDMS. Fused silica and indium tin oxide (ITO)-coated soda lime substrates were purchased from Nanoscribe GmbH & Co. KG as well and used as substrates for 2PP fabrication of the polymeric microstructures. SBB was purchased from Alfa Aesar. All other materials were purchased from Sigma-Aldrich.

2.2. Design of microstructures

Concerning auto-fluorescence and mechanical characterization measurements, pedestals of dimensions $30\times30\times20$ μm^3 (l×w×h) were designed. The only exception was the mechanical characterization of IP-PDMS structures. For these measurements, pedestals of dimensions $150\times150\times20$ μm^3 (l×w×h) were designed. For cell culture studies, rectangular microchannels (inner channel dimensions were $w\times h = 30\times30$ μm^2 and channel length = 100 μm), and 3D microcages with circular pores of 30 μm diameter and total volume of $120\times120\times120$ μm^3 were designed (see Fig. S1 in the Supporting Information). For IP-L, IP-Dip, and IP-S, the top wall thickness of the microchannels was 3 μm and the one of the intermediate wall was 4 μm while for IP-PDMS these thicknesses had to be increased to 10 μm and 18 μm, respectively, to increase structural stability due to increased shrinkage of the material.

2.3. Fabrication of microstructures

All substrates used for printing were first cleaned with acetone and isopropanol (IPA) before any treatment. Microstructures were printed using the Photonic Professional GT+ (PPGT+) 2PP printer, which is a setup of Nanoscribe GmbH & Co. KG. The printer is equipped with a pulsed femtosecond fibre laser featuring a pulse duration of roughly 80 fs, a repetition rate of 80 MHz, a wavelength of 780 nm, and a maximum power of 50 mW. IP-Dip structures were printed on fused silica substrates ($l\times w\times h = 25\times25\times0.7$ mm^3) via a 63x Zeiss objective with a numerical aperture (NA) of 1.4. IP-L, IP-S, and IP-PDMS were printed on soda lime substrates coated with ITO ($l\times w\times h = 25\times25\times0.7$ mm^3) via a 25x Zeiss objective (NA = 0.8). Printing of all structures took place in dip in laser lithography (DiLL) configuration (where the lens is immersed into the photoresin) and Galvo mode (where movement of the laser in the x-y dimensions is performed with the assistance of a set of galvanometric mirrors). Structures of all 4 materials used for cell culture were printed on silanized substrates to improve their adhesion to the substrates especially during the cell culture period since dipping the samples into cell culture medium may result in the delamination of the structures from the substrates. IP-Dip and IP-PDMS pedestals were also printed on silanized substrates for enhanced adhesion. Concerning silanization, the cleaned substrates were activated in a Diener Femto oxygen plasma cleaner at 100 W for 5 min with a flowrate of 5 cm^3/min and a pressure of ~0.2 mbar and then submerged in a 3-(Trimethoxysilyl)propyl methacrylate (MAPTMS) solution (2% *v/v* in ethanol) for 1 h. The substrates were then rinsed with acetone, blow dried with an air gun, and stored in a petri dish wrapped with parafilm away from light. All silanized substrates were used within one month after the silanization process. Directly before printing, the silanized substrates were cleaned with an acetone-wetted lint free wipe and blow dried with an air gun.

All structures were designed in SOLIDWORKS (Dassault Systemes), saved as “stl” files, and then imported into Describe (the proprietary software of Nanoscribe GmbH & Co. KG). In Describe, the structures were cut into vertical slices and horizontal hatching lines since 2PP printing is achieved in a line-by-line fashion (see Table S1 in the Supporting information for printing parameters of all structures including laser intensities [27]). After printing, IP-L, IP-Dip, and IP-S structures

were developed in propylene glycol methyl ether acetate (PGMEA) for 1 h horizontally in a glass petri dish. This was followed by 2 min of gentle stirring by hand, before submerging the samples in IPA for 5 min followed by gentle stirring by hand for 2 min. Finally, the samples were blow dried with an air gun and stored in the dark until further use. IP-PDMS structures were developed in IPA for 30 min horizontally in a glass petri dish followed by gentle stirring by hand for 2 min. Afterwards, they were moved into a fresh IPA bath for 1 min, followed by gentle stirring by hand for 2 min. The samples were then left to air dry for a few minutes and stored in the dark until further use.

2.4. Bleaching treatment

Structures were bleached by using an upright UV point source (Bluepoint 4 Ecocure Honle UV technology) at a distance of 1 cm from the sample for 2 h at 100% power. The diameter of the point source was 8 mm and had a power of 10,000 mW/cm^2 at the emitting surface. The spectrum of emission ranged from 300 to 600 nm with a maximum intensity at ~375 nm. During the exposure, the substrates were placed within an aluminium foil enclosure since the reflective properties of aluminium maximize the efficiency of UV exposure.

2.5. SBB treatment

Treatment for auto-fluorescence quenching was performed by dipping the samples in a 0.3% *w/v* solution of the fluorescence quencher SBB in 70% ethanol for 2 h [20,26]. Afterwards, the samples were rinsed multiple times with ethanol before drying with an air gun.

For IP-PDMS, an additional step of plasma pre-treatment was added to enhance the adhesion of SBB to the material. The structures were exposed to oxygen plasma at 100 W for 30 s with a flowrate of 5 cm^3/min and a pressure of ~0.2 mbar in a Diener Femto plasma cleaner. They were then directly dipped in SBB solution as already mentioned.

2.6. SEM characterization

To prepare the samples for SEM characterization, they were first sputter coated with a nanometric layer of gold using a JEOL JFC-1300 auto-fine sputter coater. A JEOL JSM-6010LA SEM (JEOL (Europe) B. V.) in high-vacuum was employed for morphological characterization.

2.7. Fluorescence measurement

Fluorescence emission spectra of the pedestals was measured by a Leica SP5 confocal microscope (Mannheim, Germany). The excitation wavelength was 405 nm. The top layer of each structure was imaged with a Leica Microsystems HC APO L 20x/1.00 W lens (NA = 1.0), in water dipping mode. The samples were submerged in deionized water while imaging. The images were taken with a scanning speed of 700 Hz at a resolution of 1024×1024 pixels and 5x zoom, resulting in a pixel size of 0.144×0.144 μm^2. The power of the laser was kept at 10% and the gain at 638 V for all measurements. The spectral range of measurement spanned from 410 to 750 nm of emission wavelength with 9.19 nm increments using a bandwidth of 10 nm. For UV-bleached samples, measurements were performed 1, 4, and 6 days after bleaching on 3 different sets of pedestals to study the effect of time on bleaching. The results of these measurements with respect to time are shown in the supporting information while the results shown in the main text are the ones acquired 1 day after bleaching.

For each sample of each material, whether untreated, photobleached or SBB-treated, the fluorescence of 5 pedestals was measured ($n = 5$). To measure the fluorescence of a pedestal, Fiji software [28] was used. First, a square of 250×250 pixels was drawn around each pedestal. The "Mean gray" value was specified then as a required measurement in the "Set Measurements" window. Using the command "Multi measure", the "Mean gray" value of each pedestal was measured at each wavelength range of emission. In addition, the background signal was evaluated by performing the same procedure, but with a 125×125 pixels drawn at a random region away from the sample. A MATLAB (MathWorks®) code was developed to analyse the data. After importing the results, the background signal was subtracted from all signals and the average of the "Mean gray" values for all 5 pedestals was calculated and then plotted against the emission wavelengths. The maximum values of auto-fluorescence were then calculated along with the standard deviation.

2.8. Mechanical characterization

To measure the Young's moduli of IP-L, IP-Dip, and IP-S before and after UV-bleaching, a FEMTOTOOLS nanomechanical testing system FT-NMT03 was employed to perform compression tests. A Si probe with a 50×50 μm^2 flat punch head able to measure a force range of 200,000 ± 0.5 μN was used for all measurements. Again, the pedestals were used for these measurements. The stiffness of UV-bleached samples were measured within 24 h from bleaching. A compression of roughly 2 μm was chosen for all pedestals. The speed of compression was 0.25 μm/s for all samples. The stiffness of 5 pedestals per material was measured before and after UV bleaching. To obtain the stiffness of each pedestal from the generated Force-Displacement curve, the slope of only the first linear part of the loading curve was evaluated using an in-house developed MATLAB code with the assistance of the polyfit function. The average stiffness was then calculated for each condition and the Young's modulus was extracted by using the equation $E = kL/A$ where E is the Young's modulus (Pa), k the stiffness (N/m), L the height of the pedestal (m), and A the area of the pedestal (m^2). The standard deviation was then calculated and the data plotted. All data analysis was performed by using the MATLAB code.

The Young's modulus of IP-PDMS was measured by nanoindentation since the material was too soft to be compressed with a FEMTOTOOLS Si probe. A Piuma Nanoindenter (Optics11 Life) was used to perform the nanoindentation. A probe of 42.7 N/m stiffness and a tip radius of 24.5 μm was employed. The depth of indentation was roughly 1 μm. As aforementioned, the IP-PDMS pedestals fabricated for this specific measurement were of 150×150×20 μm^3 (l×w×h) dimensions since the smaller pedestals used for the other 3 materials were too small for the dimensions of the probe used for nanoindentation. UV-bleached samples were measured within 24 h from bleaching. The Young's moduli of 5 pedestals of the material before and after UV bleaching were tested. The Piuma Nanoindeter modelling tool employed the Johnson-Kendall-Roberts (JKR) model for adhesive materials in order to evaluate the Young's moduli of the samples. The results were then imported into a MATLAB code to calculate the Young's moduli average and standard deviation and plot the data.

2.9. Cell culture

SH-SY5Y human neuroblastoma cells (Sigma-Aldrich, #94030304) were cultured in Dulbecco's Modified Eagle's Medium (DMEM)/F-12 media (1:1) (Thermo Fisher Scientific, #10565018) supplemented with 10% fetal bovine serum (FBS, Sigma-Aldrich F7524) and 1% penicillin/streptomycin and grown in an incubator at 37 °C, 5% CO_2. When cell confluency was reached, trypsin (×1) was used to harvest the cells and centrifuged at 900 rpm for 5 min. The microstructures (microchannels and microcages) were enclosed in a well of 1×1 cm^2 area made of polydimethylsiloxane (PDMS) and placed on the substrate. A 100 μL droplet containing 50,000 cells was seeded on all the structures within the PDMS wells placed on all samples. Following the seeding, the cells were exposed to 10 μM retinoic acid (Sigma-Aldrich, R2625) for 3 days in DMEM/F-12 media to differentiate the cells into immature neuron-like cells. Following 3 days of differentiation, cells were fixed in 4% paraformaldehyde solution for 25 min prior to staining.

2.10. Immunofluorescence staining and confocal imaging

Following fixation in 4% paraformaldehyde for 25 min, cells were permeabilized for 10 min at room temperature (RT) using 0.1% Triton X-100 in Phosphate Buffer Saline solution (PBS). Subsequently, cells were blocked for 30 min at RT using 1% bovine serum albumin (BSA) in PBS. Primary antibodies against paxillin (Sigma-Aldrich, SAB4502553) were diluted 1:200 in 1% BSA and incubated for 1.5 h at RT to visualize focal adhesions. Secondary antibody (Sigma-Aldrich, SAB3700937-Anti-Rabbit IgG (H + L)-Texas Red® antibody) was then diluted 1:500 in 1% BSA and incubated at RT for 2 h. Phalloidin staining for F-actin in the cytoskeleton was used (Thermo Fisher Scientific, ActinGreen 488 ReadyProbes, R37110). Cell nuclei were stained using Hoechst 33342 (Thermo Fisher Scientific, NucBlue Live ReadyProbes, R37605). For both actin and Hoechst, 2 drops per mL in PBS were added and incubated for 25 min. Samples were washed 3 times with PBS afterwards and stored in PBS in the dark until imaging.

Samples were imaged using a Leica SP5 confocal microscope with a Leica Microsystems HC APO L 20x/1.00 W lens (NA = 1.0) in water dipping mode. The samples were kept in PBS while imaging. Laser sources of wavelengths 405, 488, and 561 nm were employed, all at 10% power. The wavelength ranges of the emission filters were 410–475 nm, 495–550 nm, and 570–750 nm for the 405, 488, and 561 nm excitation lines, respectively. Acquisition was performed in parallel for all three channels. The gain was kept at 638 V for all images and the zoom at 3.5×. These imaging parameters were kept constant to facilitate the comparison between untreated and treated samples. *Z*-stacks were obtained at a resolution of 1024×1024 pixels, a scanning speed of 700 Hz, and a step size of 0.5 µm resulting in a pixel size of 0.206×0.206 µm^2. All z-stacks were processed using Fiji [28] or Imaris Viewer software (Oxford Instruments).

3. Results and discussion

3.1. Microstructures fabrication

Two-photon polymerized pedestals were fabricated using 4 different commercial acrylate resins. Optical microscope images of the fabricated pedestals are shown in Fig. 1. As aforementioned, the 4 materials are IP-L (Fig. 1a), IP-Dip (Fig. 1b), IP-S (Fig. 1c) and IP-PDMS (Fig. 1d). Minimal shrinkage was observed for the pedestals. These structures were used for fluorescence and mechanical characterization. Fig. 2 shows representative SEM images of the 3D structures fabricated for cell culture studies. The images shown are only of IP-L (Fig. 2a,b) and IP-PDMS (Fig. 2c,d). These structures included rectangular microchannels and 3D free standing microcages made of periodic circular pores. Both structures posed no problems when fabricated with IP-L, IP-Dip, or IP-S even with a 3 µm thick wall of the channels. When employing IP-PDMS, however, this wall thickness turned out to be too thin to withstand the significant shrinkage of this specific resin. Therefore, the top wall thickness of the channels had to be increased to 10 µm and the intermediate wall thickness to 18 µm to guarantee a high enough structural integrity. Additionally, the 3D microcages shrunk substantially and showed some minor deformations compared to those made of IP-L, IP-Dip, or IP-S. No changes to the design of the microcages were necessary however.

3.2. Auto-fluorescence suppression

In order to suppress the auto-fluorescence of all IP materials, the effect of bleaching versus coating with SBB (an auto-fluorescence quencher) was assessed. All materials were bleached by a UV point source for 2 h or treated by submerging in a solution of SBB for 2 h. The UV point source had an emission range of 300–600 nm as mentioned previously (section 2.4). This range of emission guaranteed the excitation of the photoinitiators within the photoresins under investigation

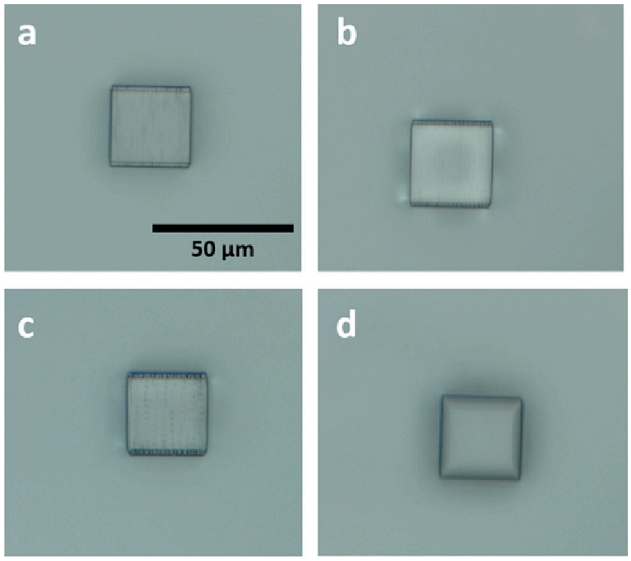

Fig. 1. Optical microscopy images of (a) IP-L pedestal, (b) IP-Dip pedestal, (c) IP-S pedestal, and (d) IP-PDMS pedestal.

since their peak absorption wavelength is at roughly 390 nm. Moreover, the specific choice of the UV point source was dictated by the fact that one of the main points of the study is to provide an easy-to-use, efficient and inexpensive method for suppressing the auto-fluorescence of 2PP-fabricated microstructures.

Fig. 3 shows representative optical microscope images of IP-L (Fig. 3a-d) and IP-PDMS (Fig. 3e-j) printed structures before and after treatment with SBB. The morphology of bleached structures did not show a significant change from the untreated ones (data not shown). After treatment with SBB, a noticeable black tint of the IP-L structures can be observed indicating the deposition of SBB on top of them (Fig. 3b, d). These results were similar to those of IP-Dip and IP-S structures (see Fig. S2 in the Supporting Information). The case for IP-PDMS was not the same since SBB adhered very poorly to these structures upon submerging them in the solution without any prior treatment (Fig. 3f,i). A possible reason for this maybe the fact that IP-PDMS structures are more hydrophobic than the other materials leading to the formation of a meniscus of the solvent at the surface of the structures thereby hindering the SBB from coming into contact with the IP-PDMS. Another reason could be a significant inertness and/or smoothness of the surfaces of structures fabricated with IP-PDMS compared to the other resins. To test the validity of these hypotheses, we treated the IP-PDMS structures with oxygen plasma for 30 s prior to submerging them in the SBB solution. The results showed a significant enhancement in the deposition and adherence of SBB to the IP-PDMS structures indicated by the darker colour observed in the treated structures (Fig. 3 g,j). Hence, we conclude that increasing the hydrophilicity, reactivity, and surface roughness of the IP-PDMS structures can lead to better interaction with SBB. It should be noted that SEM images of IP-L and IP-PDMS structures were taken before and after SBB treatment (see Fig. S3 in the Supporting information). However, it was impossible to recognize any morphological difference between the treated and untreated samples.

The effect of both treatment methods on the auto-fluorescence of all 4 materials is shown in Fig. 4. The structures used for the comparison shown in Fig. 4 were pedestals (see the Materials and Methods section for more details). For each configuration (i.e. control, bleached, SBB treated, and plasma+SBB treated), the emission spectra of 5 pedestals were measured (n = 5). All results are shown as relative auto-fluorescence intensity (I) with a 100% denoting the highest signal value among all configurations for one specific material. A comparison between the auto-fluorescence of all materials over a wavelength spectrum of 410 to 750 nm clearly showed that IP-Dip is the most auto-

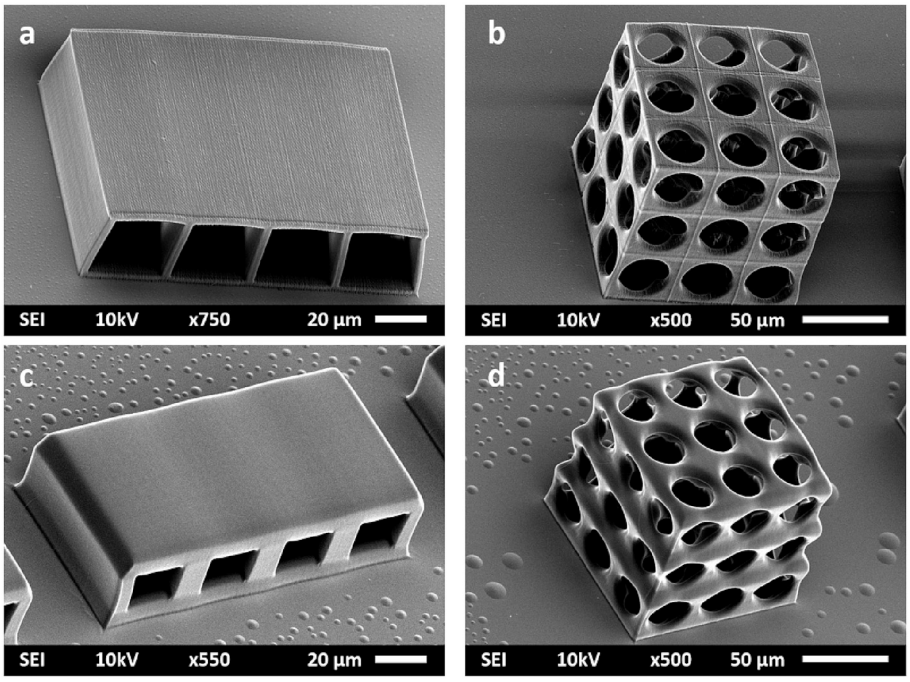

Fig. 2. Representative SEM images of (a) IP-L rectangular microchannels, (b) IP-L microcage, (c) IP-PDMS rectangular microchannels, and (d) IP-PDMS microcages.

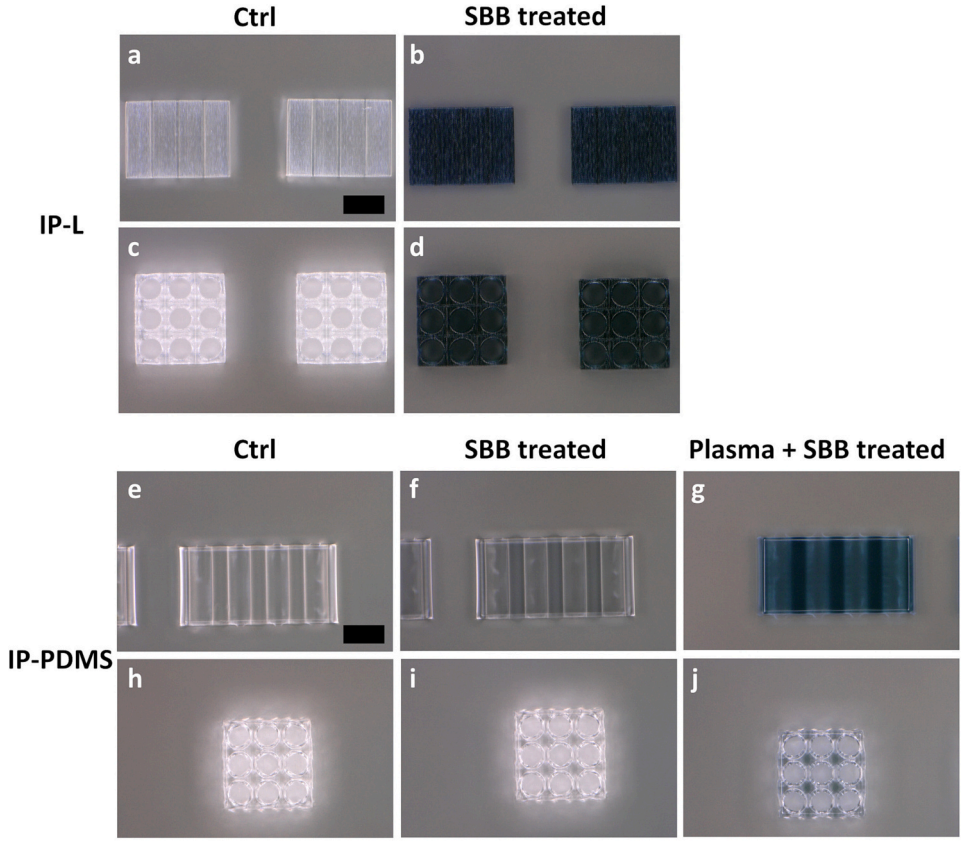

Fig. 3. Optical microscope images of (a,c) untreated IP-L fabricated structures (i.e. controls), (b,d) SBB treated IP-L structures, (e,h) untreated IP-PDMS fabricated structures, (f,i) SBB treated IP-PDMS fabricated structures, (g,j) IP-PDMS structures pre-treated with oxygen plasma for 30 s and then treated with SBB. Scale bar = 50 µm.

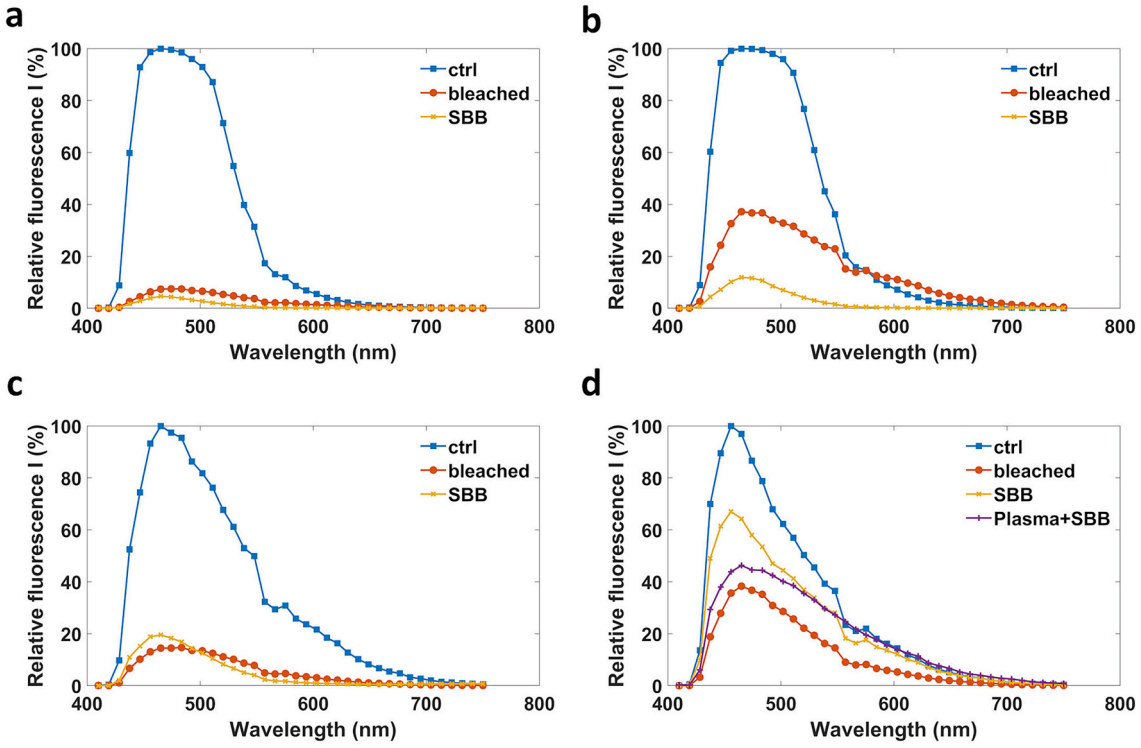

Fig. 4. Relative auto-fluorescence intensity (I) of treated and untreated structures made of respectively (a) IP-L, (b) IP-Dip, (c) IP-S, and (d) IP-PDMS. For each condition $n = 5$ pedestals.

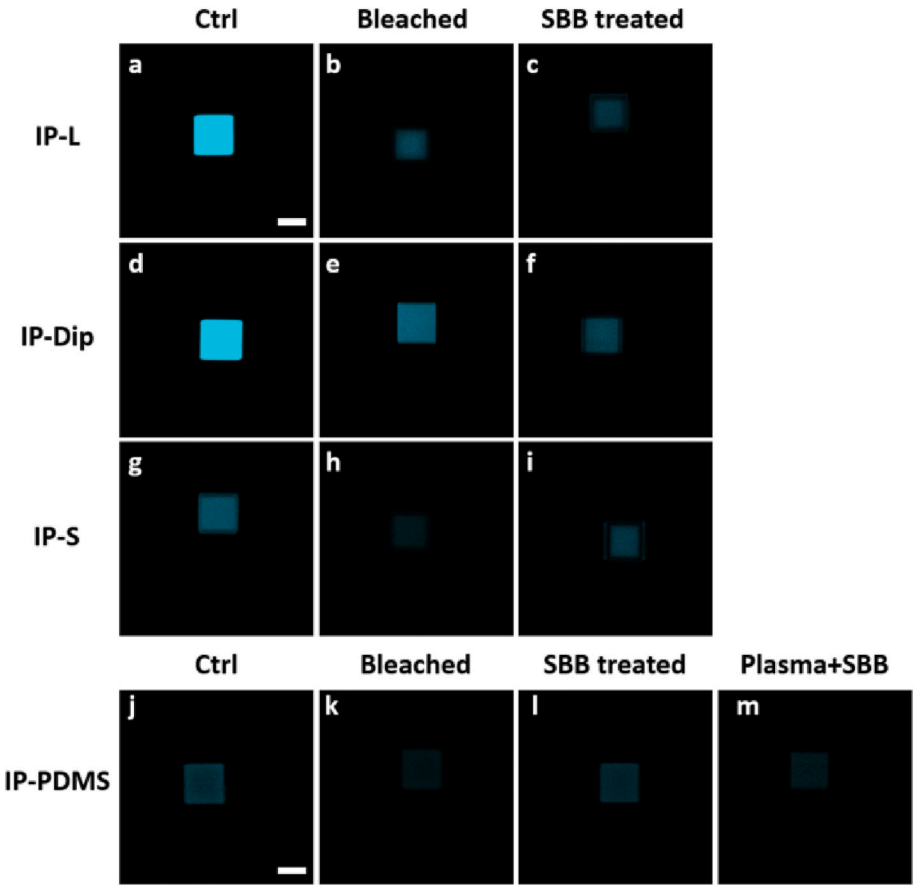

Fig. 5. Confocal microscopy images of the top layer of the pedestals fabricated from IP-L (a-c), IP-Dip (d-f), IP-S (g-i), and IP-PDMS (j-m). The effect of bleaching and SBB treatment is shown for each material. All images were acquired at an emission wavelength range of 465–475 nm (the wavelength range at which the auto-fluorescence signal was maximum). Scale bar = 20 μm.

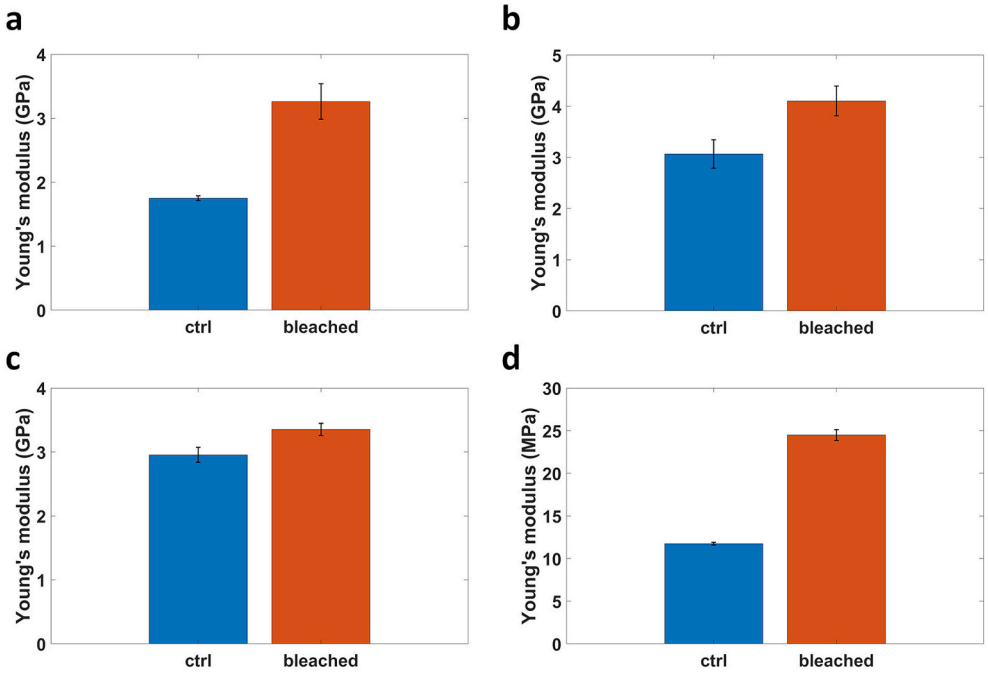

Fig. 6. A comparison of the Young's moduli of untreated (control) samples versus bleached samples of (a) IP-L, (b) IP-Dip, (c) IP-S, and (d) IP-PDMS. For each condition $n = 5$ pedestals.

fluorescent among all four materials (see Fig. S4 in the Supporting information). The wavelength range at which the signal is maximal for all materials was 465–475 nm. In general, it can be concluded that all materials are highly fluorescent in the blue (400–500 nm) and green (500–600 nm) channels especially, while the fluorescence tapers off towards the red region of the spectrum (600–800 nm). The difference in signal intensity between IP-Dip and other materials may be attributed to the type of photoinitiators used in combination with the different printing parameters employed for each material. Fig. 4a indicates the effect of bleaching and SBB treatment on IP-L structures. Both treatments turned out to be very effective in eliminating fluorescence, but the SBB treatment was slightly more effective. Bleaching decreased the maximum fluorescence intensity by 92.5% ± 0.5 while SBB decreased it by 95.4% ± 0.7.

For IP-Dip, the reduction in maximum fluorescence with bleaching turned out to be 62.8% ± 10.2 while with SBB treatment it was 88% ± 4.2 (Fig. 4b). An interesting observation, in the data reported in Fig. 4b, is that the bleached sample seems to have a slightly higher auto-fluorescence than the control in the spectral region of 575–750 nm. A similar phenomenon, known as photoconversion, is an invaluable tool in the fields of single-molecule super resolution imaging and dynamic imaging. This mechanism is observed for multiple fluorescent proteins (FPs) such as mKate (which is converted from red to green fluorescence) [29,30] and Dendra2 (which is converted from green to red fluorescence) [31]. In the context of our investigation, we hypothesize that the increase in fluorescence in the red region of the spectrum for IP-Dip may indicate the creation of new fluorescent species as a result of photobleaching. This hypothesis is supported by the fact that the auto-fluorescent component of IP-Dip is the photoinitiator. Therefore, bleaching may be cleaving the molecules of the photoinitiator and creating other molecules with different conformations that results in their increased fluorescence in the red part of the spectrum while simultaneously decreasing their fluorescence in the blue-green region of the spectrum [31]. Although we cannot ultimately conclude if our observations are directly correlated to the photoconversion phenomenon, to the best of our knowledge, this is the first time that this behaviour is reported for a photosensitive resin.

As for IP-S, bleaching was 85.3% ± 2.1 effective while SBB showed a comparable result of 80.5% ± 2.6 (Fig. 4c). For IP-PDMS on the other hand, bleaching was 61.7% ± 2.3 effective while SBB was only 33% ± 1.5 effective (Fig. 4d). The reason for such a small effect of SBB may be attributed to the poor adhesion of the material on the surface of IP-PDMS structures. Upon examining structures that were pre-treated with plasma, the efficiency of SBB increased to 53.7% ± 10.4 confirming the improved adhesion of SBB to the structures. These results show on average that the two solutions are comparable for all four materials. Fig. 5 shows representative confocal microscopy images of the top layer of the pedestals of all materials with and without the mentioned treatments. All images were taken at an emission wavelength range of 465–475 nm which corresponds to the maximum intensity of auto-fluorescence signal for all materials. The images clearly show the reduction in auto-fluorescence upon employing UV-bleaching or SBB treatment.

In addition to this investigation, we conducted a study to determine the effect of aging after bleaching the auto-fluorescence of the materials. It has been shown for some FPs, such as Cyan fluorescent proteins, that regaining fluorescence is possible after bleaching if they are kept in a dark environment for a short amount of time [32]. For this reason, we assessed the auto-fluorescence signal after 1, 4, and 6 days of UV-bleaching. Different samples were used for each day. The results showed no significant change in the auto-fluorescence signal with respect to time (see Fig. S5 in the Supporting information).

3.3. *Mechanical characterization*

The Young's moduli (E) of all four materials before and after bleaching were measured by compression testing (for IP-L, IP-Dip, and IP-S) or nanoindentation (for IP-PDMS). Fig. 6 shows the change in E for all materials. For IP-L, E was evaluated to be 1.75 GPa ± 0.04 for the control sample and 3.26 GPa ± 0.28 for the bleached one (Fig. 6a). As for IP-Dip, E increased from 3.07 GPa ± 0.28 for the control sample to 4.1 GPa ± 0.29 for the bleached sample (Fig. 6b). For IP-S, E increased from 2.95 GPa ± 0.12 to 3.35 GPa ± 0.09 for the control and bleached samples respectively (Fig. 6c).

The Young's modulus of IP-PDMS increased approximately two fold from 11.74 MPa ± 0.16 for the control to 24.5 MPa ± 0.63 for the

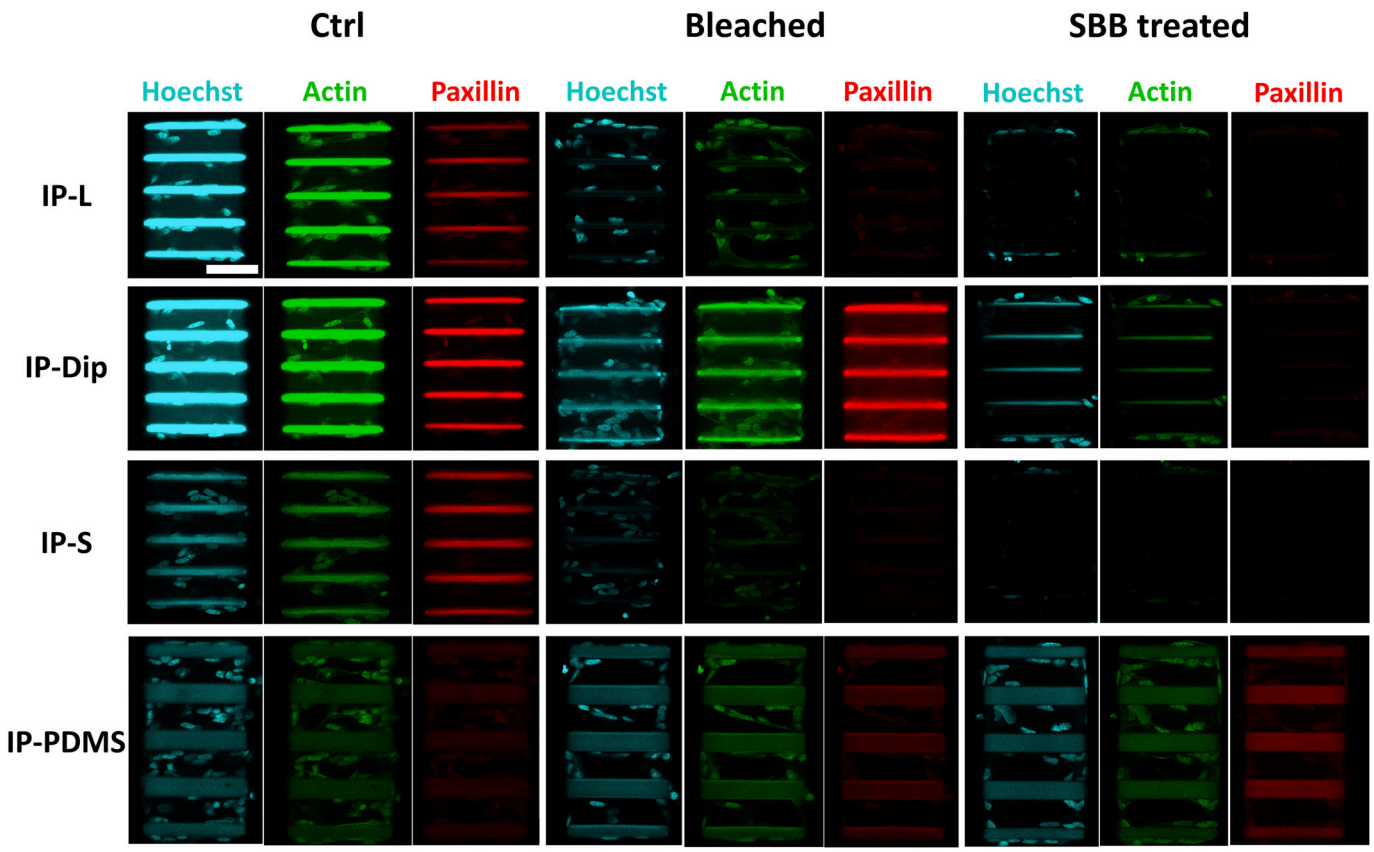

Fig. 7. Confocal images of differentiated and stained SH-SY5Y cells in the 3D rectangular microchannels. The depicted images are from the mid-section of the rectangular microchannels. Blue is Hoechst staining (cells nuclei). Green is actin (cytoskeleton). Red is paxillin (focal adhesions). All images were taken at the same laser power and gain. These images were processed by Fiji. Scale bar = 50 μm. (For interpretation of the references to colour in this figure legend, the reader is referred to the web version of this article.)

bleached samples (Fig. 6d). The increase in E is not surprising since the photoinitiator and some residual monomers remain within the solid structures even after development. Exposure to a UV light source excites these photoinitiaor molecules thus resuming the polymerization and crosslinking reaction leading to a stiffer structure with more crosslinks and a higher elastic modulus. This characterization is important as the elastic modulus of a biomaterial can have an influence on cell fate [33,34]. It is noteworthy that the mechanical characterization was only carried out for UV bleached samples and not SBB-treated ones owing to the fact that SBB treatment is a mere surface treatment resulting in the deposition of a nanometric layer on the surface of the structures. Therefore, SBB treatment is not expected to affect any of the intrinsic mechanical properties of the materials.

3.4. *Visualization of stained cells*

In order to validate our results in the context of cell biology applications, we conducted a study in which the proposed fluorescence suppression solutions were employed on the materials cultured with SH-SY5Y human neuroblastoma cells. The cells were cultured on the control and treated structures, differentiated for 3 days, and then stained for Hoechst (blue nucleus staining), phalloidin (green actin staining for the cytoskeleton), and paxillin (red staining for visualization of focal adhesions). Fig. 7 shows a comparison between the results for cells cultured in the 3D rectangular microchannels. The intermediate section of the structure along the z-axis is shown in the figure in the blue, green, and red channels. All imaging acquisitions represented in Fig. 7 were performed using the same laser power and gain. We associate any overlap that maybe observed in the emission of the green and blue channels to the fact that the acquisition was performed in parallel for all three channels (blue, green, and red). All treated polymeric structures enabled a significant enhancement in visualization of the cells. Nonetheless, bleached structures showed to be superior to SBB coated ones since the SBB absorbed the fluorescence of the staining of the cells. This explanation is supported by the fact that the peak emissions of Hoechst 33342, ActinGreen 488, and Texas Red are 460, 518, and 615 nm, respectively, which clearly fall well within the spectral region of absorption of SBB [35]. The only material for which SBB did not cause such a problem was IP-PDMS due to the poor adhesion of the SBB to that specific material. To further illustrate the difference between untreated and treated microchannels in terms of cell visualization, we show representative 3D reconstructions of the structures in Fig. S6 and zoomed-in images of the intermediate sections of the microchannels in Fig. S7, acquired at optimized imaging parameters for each configuration, in the supporting information. The obtained results reveal that for SBB-treated materials, except for IP-PDMS, the laser power had to be increased to more than 50% to be able to visualize the cells and even then, the gain had to be increased to a degree where background noise obstructed efficient visualization of the stainings. This was especially a problem when visualizing paxillin (in the red channel) since focal adhesions can be a few hundred nanometres in size and increased noise substantially affects their measurement. Moreover, for IP-S for example, the microstructures were damaged when increasing the laser power of the 405 nm wavelength laser to 50% (data not shown).

Additionally, as already indicated previously, after bleaching, autofluorescence of IP-Dip decreased in the blue and green channels, but increased in the red channel, rendering the visualization of cells in that channel very difficult. Fig. S8 in the supporting information also depicts representative images of the intermediate section of treated and untreated microchannels acquired sequentially instead of in parallel for

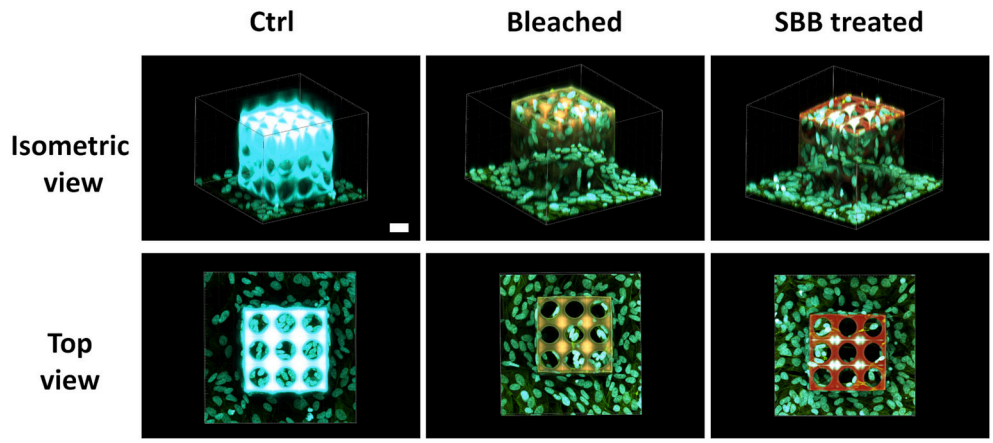

Fig. 8. 3D reconstruction of IP-L microcages with differentiated SH-SY5Y cells cultured on them. The images represent merged blue, green, and red channels. Blue is Hoechst staining (cells nuclei). Green is actin (cytoskeleton). Red is paxillin (focal adhesions). The top row shows an isometric view of the cages and the bottom one shows the top view. All z-stacks were acquired at the same laser power and gain. These images were created by Imaris Viewer software. Scale bar = 30 μm. (For interpretation of the references to colour in this figure legend, the reader is referred to the web version of this article.)

blue, green, and red channels. The observations made earlier were similar for images acquired via sequential scanning.

To further assess the efficiency of both solutions, SH-SY5Y cells were also cultured on 3D microcages and differentiated for 3 days as shown in Fig. 8. The structures represented in the figure are of IP-L only. All structures were imaged using the same laser power and gain to facilitate the comparison. The acquisition was obtained via parallel scanning for all three channels (blue, green, and red). A clear difference can be observed in Fig. 8 between the untreated structure and the treated ones as the strong auto-fluorescence of the untreated structure especially in the blue channel hinders any meaningful analysis of cells within this complex 3D structure. Bleached and SBB-treated structures on the other hand showed a significant enhancement in visualization of the cells due to the decreased auto-fluorescence. Using these imaging parameters (i.e. laser power and gain), no substantial difference between bleached or SBB-treated structures was noticed. However, upon attempting to optimize the imaging parameters to better visualize the middle and lower sections of the microcages, once again, SBB proved to be inferior to bleaching as the laser power had to be increased to 50% which resulted in substantial background noise (see Fig. S9 in the Supporting Information). It must be noted though that the results for bleached structures were not perfect due to the high structural density of the microcages, which results in scattering and absorbing emitted photons from the lower sections of the structure. An additional acquisition via sequential scanning of blue, green, and red channels of the microcages is shown in Fig. S10 in the supporting information to illustrate that the reported observations apply to that modality of confocal acquisition as well.

These results lead us to conclude that although both methods are effective in suppressing the auto-fluorescence of various materials, the preference of one over the other highly depends on the geometry of the structure. In our cell culture study, SBB coating did not perform as well as bleaching. It should be noted however that bleaching is also not a perfect solution since it can lead to unexpected behaviours like the increased auto-fluorescence of IP-Dip in the red region of the spectrum. Both solutions provide anyhow a path towards the suppression of auto-fluorescence of 2PP scaffolds.

4. Conclusion

In the present study, we address the issue of auto-fluorescence of four commercial photoresins that are widely used in the field of 2PP. In the context of *in vitro* mechanobiological studies that involve the fabrication of 3D microscaffolds, auto-fluorescence of these structures interfere with the analysis of cells cultured onto them. Therefore, we proposed a systematic study and comparison between two solutions for the supression of auto-fluorescence that are applied after the fabrication of the structures, namely, photo-bleaching and auto-fluorescence quenching. The proposed solutions can be performed with relative ease and with virtually any material, therefore they are not limited by the current selection of materials. Our results show that photo-bleaching consistently eliminates the auto-fluorescence of all materials and does not depend on the chemistry of the material. In some cases (such as with IP-Dip), it can result in the creation of a species that slightly increases the auto-fluorescence of the material in one region of the spectrum while simultaneously decreasing it in another region. Concerning quenching instead, we used SBB to coat the surface of the structures and obstruct photons emitted by them. SBB proved to be of equal efficiency or superior to bleaching with all materials used for this study except for IP-PDMS where it only reduced the fluorescence by 33%. This is attributed to the affinity of SBB to be adsorbed by one material rather than the other. Such affinity is likely affected by the hydrophobicity/philicity, charges, and roughness of a surface in relation to SBB. With an oxygen plasma pre-treatment, however, the IP-PDMS structures were activated and SBB achieved better adhesion resulting in a significant increase in auto-fluorescence suppression. In addition, we performed a study with human neuroblastoma cell line (SH-SY5Y) to emphasize the efficiency of both solutions and compared them. Our results showed that bleaching is superior to quenching in the proposed scenarios, since in the case of rectangular microchannels and microcages within which cells migrate, SBB quenches not only the fluorescence of the structures, but also that of the stained cells inside the structures. Therefore, the choice of either one of these two solutions highly depends on the type of experiments planned and structures used. In summary, the present study provides a systematic comparison of solutions to suppress the auto-fluorescence of two-photon polymerized microstructures in order to increase the efficiency of analysis using fluorescence microscopy for cell biology applications.

Author contributions

A.S designed, fabricated and characterized the 2PP microstructures. J.P.F. performed the cells experiments and commented on the manuscript. G.J.K. assisted with the confocal imaging and commented on the manuscript. A.S. wrote the initial draft of the manuscript. A.A. conceived and supervised the project and reviewed and edited the manuscript. All authors facilitated the discussion of the results, edited the manuscript and approved the submitted version.

Data availability

Data will be made available on request.

Acknowledgements

A.S. acknowledges the financial support from Delft University of Technology. This work was also supported by the Netherlands Organ-on-

Chip Initiative, an NWO Gravitation project (024.003.001) funded by the Ministry of Education, Culture and Science of the government of the Netherlands.

Appendix A. Supplementary data

Supplementary data to this article can be found online at https://doi.org/10.1016/j.mne.2023.100188.

References

[1] F. Rey, B. Barzaghini, A. Nardini, M. Bordoni, G.V. Zuccotti, C. Cereda, M. T. Raimondi, S. Carelli, Advances in tissue engineering and innovative fabrication techniques for 3-D-structures: translational applications in neurodegenerative diseases, Cells. 9 (2020) 1636, https://doi.org/10.3390/cells9071636.

[2] A. Lambert, S. Valiulis, Q. Cheng, Advances in optical sensing and bioanalysis enabled by 3D printing, ACS Sens. 3 (2018) 2475–2491, https://doi.org/10.1021/acssensors.8b01085.

[3] S. Waheed, J.M. Cabot, N.P. Macdonald, T. Lewis, R.M. Guijt, B. Paull, M. C. Breadmore, 3D printed microfluidic devices: enablers and barriers, Lab Chip 16 (2016) 1993–2013, https://doi.org/10.1039/C6LC00284F.

[4] L.C. Ransanz, P.F. Van Altena, V.M. Heine, A. Accardo, Engineered cell culture microenvironments for mechanobiology studies of brain neural cells, Front. Bioeng. Biotechnol. 10 (2022) (2022) 1096054, https://doi.org/10.3389/fbioe.2022.1096054.

[5] A. Accardo, C. Cirillo, S. Lionnet, C. Vieu, I. Loubinoux, Interfacing cells with microengineered scaffolds for neural tissue reconstruction, Brain Res. Bull. 152 (2019) 202–211, https://doi.org/10.1016/j.brainresbull.2019.07.020.

[6] D. Kim, S.-M. Kim, S. Lee, M.-H. Yoon, Investigation of neuronal pathfinding and construction of artificial neuronal networks on 3D-arranged porous fibrillar scaffolds with controlled geometry, Sci. Rep. 7 (2017) 7716, https://doi.org/10.1038/s41598-017-08231-3.

[7] R.L. Wilmoth, V.L. Ferguson, S.J. Bryant, A 3D, dynamically loaded hydrogel model of the osteochondral unit to study osteocyte Mechanobiology, Adv. Healthcare Mater. 9 (2020) 2001226, https://doi.org/10.1002/adhm.202001226.

[8] G. Silvani, C. Basirun, H. Wu, C. Mehner, K. Poole, P. Bradbury, J. Chou, A 3D-bioprinted vascularized glioblastoma-on-a-Chip for studying the impact of simulated microgravity as a novel pre-clinical approach in brain tumor therapy, Adv. Therapeut. 4 (2021) 2100106, https://doi.org/10.1002/adtp.202100106.

[9] E.D. Lemma, B. Spagnolo, M. De Vittorio, F. Pisanello, Studying cell Mechanobiology in 3D: the two-photon lithography approach, Trends Biotechnol. 37 (2019) 358–372, https://doi.org/10.1016/j.tibtech.2018.09.008.

[10] M. Malinauskas, A. Žukauskas, G. Bičkauskaitė, R. Gadonas, S. Juodkazis, Mechanisms of three-dimensional structuring of photo-polymers by tightly focussed femtosecond laser pulses, Opt. Express, OE. 18 (2010) 10209–10221, https://doi.org/10.1364/OE.18.010209.

[11] M. Emons, K. Obata, T. Binhammer, A. Ovsianikov, B.N. Chichkov, U. Morgner, Two-photon polymerization technique with sub-50 nm resolution by sub-10 fs laser pulses, Opt. Mater. Express, OME. 2 (2012) 942–947, https://doi.org/10.1364/OME.2.000942.

[12] A. Sharaf, R. Timmerman, J. Bajramovic, A. Accardo, *In vitro* microglia models: the era of engineered cell microenvironments, Neural Regen. Res. 18 (8) (2023) 1709–1710, https://doi.org/10.4103/1673-5374.363828.

[13] Q. Akolawala, M. Rovituso, H.H. Versteeg, A.M.R. Rondon, A. Accardo, Evaluation of proton-induced DNA damage in 3D-engineered glioblastoma microenvironments, ACS Appl. Mater. Interfaces (2022), https://doi.org/10.1021/acsami.2c03706.

[14] B.N.L. Costa, R.M.R. Adão, C. Maibohm, A. Accardo, V.F. Cardoso, J.B. Nieder, Cellular interaction of bone marrow mesenchymal stem cells with polymer and hydrogel 3D microscaffold templates, ACS Appl. Mater. Interfaces (2022), https://doi.org/10.1021/acsami.1c23442.

[15] M. Hippler, K. Weißenbruch, K. Richler, E.D. Lemma, M. Nakahata, B. Richter, C. Barner-Kowollik, Y. Takashima, A. Harada, E. Blasco, M. Wegener, M. Tanaka, M. Bastmeyer, Mechanical stimulation of single cells by reversible host-guest interactions in 3D microscaffolds, science, Advances. 6 (2020) eabc2648, https://doi.org/10.1126/sciadv.abc2648.

[16] A. Sharaf, B. Roos, R. Timmerman, G.-J. Kremers, J.J. Bajramovic, A. Accardo, Two-photon polymerization of 2.5D and 3D microstructures fostering a ramified resting phenotype in primary microglia, Front. Bioeng. Biotechnol. 10 (2022), https://doi.org/10.3389/fbioe.2022.926642.

[17] N. Barin, H.E. Balcioglu, I. de Heer, M. de Wit, M.L.M. Lamfers, M.E. van Royen, P. J. French, A. Accardo, 3D-engineered scaffolds to study microtubes and localization of epidermal growth factor receptor in patient-derived glioma cells, Small. 18 (2022) 2204485, https://doi.org/10.1002/smll.202204485.

[18] J. Maciulaitis, S. Rekštytė, M. Bratchikov, R. Gudas, M. Malinauskas, A. Pockevicius, A. Usas, A. Rimkunas, V. Jankauskaite, V. Grigaliunas, R. Maciulaitis, Customization of direct laser lithography-based 3D scaffolds for optimized *in vivo* outcome, Appl. Surf. Sci. 487 (2019) 692–702, https://doi.org/10.1016/j.apsusc.2019.05.065.

[19] E.D. Lemma, S. Sergio, B. Spagnolo, M. Pisanello, L. Algieri, M.A. Coluccia, M. Maffia, M. De Vittorio, F. Pisanello, Tunable mechanical properties of stent-like microscaffolds for studying cancer cell recognition of stiffness gradients, Microelectron. Eng. 190 (2018) 11–18, https://doi.org/10.1016/j.mee.2018.01.007.

[20] G. Flamourakis, G. Flamourakis, A. Kordas, A. Kordas, G.D. Barmparis, A. Ranella, A. Ranella, M. Farsari, M. Farsari, Low-autofluorescence, transparent composite for multiphoton 3D printing, Opt. Mater. Express, OME. 11 (2021) 801–813, https://doi.org/10.1364/OME.418269.

[21] M. Nouri-Goushki, A. Isaakidou, B.I.M. Eijkel, M. Minneboo, Q. Liu, P.E. Boukany, M.J. Mirzaali, L.E. Fratila-Apachitei, A.A. Zadpoor, 3D printed submicron patterns orchestrate the response of macrophages, Nanoscale. 13 (2021) 14304–14315, https://doi.org/10.1039/D1NR01557E.

[22] A. Accardo, M.-C. Blatché, R. Courson, I. Loubinoux, C. Vieu, L. Malaquin, Direct laser fabrication of free-standing PEGDA-hydrogel scaffolds for neuronal cell growth, Mater. Today 21 (2018) 315–316, https://doi.org/10.1016/j.mattod.2018.02.004.

[23] S. Turunen, T. Joki, M.L. Hiltunen, T.O. Ihalainen, S. Narkilahti, M. Kellomäki, Direct laser writing of tubular microtowers for 3D culture of human pluripotent stem cell-derived neuronal cells, ACS Appl. Mater. Interfaces 9 (2017) 25717–25730, https://doi.org/10.1021/acsami.7b05536.

[24] A. Marino, G. Ciofani, C. Filippeschi, M. Pellegrino, M. Pellegrini, P. Orsini, M. Pasqualetti, V. Mattoli, B. Mazzolai, Two-photon polymerization of sub-micrometric patterned surfaces: investigation of cell-substrate interactions and improved differentiation of neuron-like cells, ACS Appl. Mater. Interfaces 5 (2013) 13012–13021, https://doi.org/10.1021/am403895k.

[25] A. Maggi, H. Li, J.R. Greer, Three-dimensional nano-architected scaffolds with tunable stiffness for efficient bone tissue growth, Acta Biomater. 63 (2017) 294–305, https://doi.org/10.1016/j.actbio.2017.09.007.

[26] I.H. Jaafar, C.E. LeBlon, M.-T. Wei, D. Ou-Yang, J.P. Coulter, S.S. Jedlicka, Improving fluorescence imaging of biological cells on biomedical polymers, Acta Biomater. 7 (2011) 1588–1598, https://doi.org/10.1016/j.actbio.2010.12.007.

[27] E. Skliutas, M. Lebedevaite, E. Kabouraki, T. Baldacchini, J. Ostrauskaite, M. Vamvakaki, M. Farsari, S. Juodkazis, M. Malinauskas, Polymerization mechanisms initiated by spatio-temporally confined light, Nanophotonics. 10 (2021) 1211–1242, https://doi.org/10.1515/nanoph-2020-0551.

[28] J. Schindelin, I. Arganda-Carreras, E. Frise, V. Kaynig, M. Longair, T. Pietzsch, S. Preibisch, C. Rueden, S. Saalfeld, B. Schmid, J.-Y. Tinevez, D.J. White, V. Hartenstein, K. Eliceiri, P. Tomancak, A. Cardona, Fiji: an open-source platform for biological-image analysis, Nat. Methods 9 (2012) 676–682, https://doi.org/10.1038/nmeth.2019.

[29] G.-J. Kremers, K.L. Hazelwood, C.S. Murphy, M.W. Davidson, D.W. Piston, Photoconversion in orange and red fluorescent proteins, Nat. Methods 6 (2009) 355–358, https://doi.org/10.1038/nmeth.1319.

[30] E.A. Protasova, A.S. Mishin, K.A. Lukyanov, E.G. Maksimov, A.M. Bogdanov, Chromophore reduction plus reversible photobleaching: how the mKate2 "photoconversion" works, Photochem. Photobiol. Sci. 20 (2021) 791–803, https://doi.org/10.1007/s43630-021-00060-8.

[31] B. Turkowyd, A. Balinovic, D. Virant, H.G.G. Carnero, F. Caldana, M. Endesfelder, D. Bourgeois, U. Endesfelder, A general mechanism of Photoconversion of green-to-red fluorescent proteins based on blue and infrared light reduces Phototoxicity in live-cell single-molecule imaging, Angew. Chem. Int. Ed. 56 (2017) 11634–11639, https://doi.org/10.1002/anie.201702870.

[32] D. Sinnecker, P. Voigt, N. Hellwig, M. Schaefer, Reversible Photobleaching of enhanced green fluorescent proteins, Biochemistry. 44 (2005) 7085–7094, https://doi.org/10.1021/bi047881x.

[33] S. Khetan, M. Guvendiren, W.R. Legant, D.M. Cohen, C.S. Chen, J.A. Burdick, Degradation-mediated cellular traction directs stem cell fate in covalently crosslinked three-dimensional hydrogels, Nat. Mater. 12 (2013) 458–465, https://doi.org/10.1038/nmat3586.

[34] T.-Y. Chang, C. Chen, M. Lee, Y.-C. Chang, C.-H. Lu, S.-T. Lu, D.-Y. Wang, A. Wang, C.-L. Guo, P.-L. Cheng, Paxillin facilitates timely neurite initiation on soft-substrate environments by interacting with the endocytic machinery, ELife. 6 (2017), e31101, https://doi.org/10.7554/eLife.31101.

[35] A.J.G. Otuka, B.B.M. Torres, J. Dipold, D.T. Balogh, V. Tribuzi, L. De Boni, C. R. Mendonça, Three-dimensional structures fabricated after laser-induced free radical generation in azoaromatic compounds, Optical Materials Express. 10 (8) (2020) 1792–1800, https://doi.org/10.1364/OME.397716.